

# Quantification of wall shear stress in large blood vessels using magnetic resonance imaging

N. SHOKINA<sup>1,\*</sup>, G. TESCHNER<sup>2</sup>, A. BAUER<sup>3</sup>, C. TROPEA<sup>3</sup>, H. EGGER<sup>2</sup>, J. HENNIG<sup>1</sup>, A.J. KRAFFT<sup>1</sup>

<sup>1</sup>Department of Radiology, Medical Physics, Medical Center — University of Freiburg, Faculty of Medicine, University of Freiburg, Freiburg, Germany

<sup>2</sup>Institute for Numerical Analysis and Scientific Computing, Department of Mathematics, Technische Universität Darmstadt, Germany

<sup>3</sup>Institute for Fluid Mechanics and Aerodynamics, Department of Mechanical Engineering, Technische Universität Darmstadt, Darmstadt, Germany

\*Corresponding author: Shokina, Nina, e-mail: [nina.shokina@uniklinik-freiburg.de](mailto:nina.shokina@uniklinik-freiburg.de)

Wall shear stress (WSS) quantifies the frictional force that flowing blood exerts on a vessel wall. Magnetic Resonance Imaging (MRI) enables non-invasive measurements of blood flow velocities that are needed for WSS computation. An introduction into MRI-based WSS quantification in large blood vessels is presented. The possible role of WSS as a potential biomarker in cardiovascular diseases, cardiovascular MRI, MR-based WSS quantification methods, and their accuracy and validation are considered. As an example, the generic nonlinear regression method for MRI-derived WSS quantification in fully developed turbulent stationary pipe flows is presented. The new method is a fully automatic and fast local WSS estimator, which produces accurate estimates independent from the spatial resolution of the measurement and may serve as a reliable reference for validation of more generic WSS estimators prior to their clinical applications.

*Keywords:* medical imaging, magnetic resonance imaging, phase-contrast MRI, wall shear stress, flow MRI, MR velocimetry, Clauser plot method.

*Cite:* Shokina, N., Teschner, G., Bauer, A., Tropea, C., Egger, H., Hennig, J., Krafft, A.J. Quantification of wall shear stress in large blood vessels using magnetic resonance imaging // Computational Technologies. 2019. Vol. 24, No. 4. P. 4–27. DOI: 10.25743/ICT.2019.24.4.002.

## Introduction

Information about normal and abnormal patterns of blood flow in the human cardiovascular system may help to discover complex pathophysiological mechanisms leading to cardiovascular diseases [1]. Depending on the clinical indications, the quantification of basic flow parameters, such as flow volume, retrograde flow, peak velocity, or advanced analysis parameters, such as wall shear stress, pulse wave velocity, kinetic energy, turbulent kinetic energy, provide valuable insights for prediction and treatment of cardiac and vascular diseases [2].

Wall shear stress (WSS) quantifies the frictional force that flowing blood exerts on a vessel wall. WSS increases with blood flow rate and is sensed principally by endothelial cells, located at the interface between blood and vessel wall [3]. Changes in WSS may eventually lead to transformations in the vessel wall, and vascular abnormalities, such as aneurysms, atherosclerosis, and stenosis, can be observed in situations where local flows are altered [3]. WSS has been suggested as a potential biomarker in various cardiovascular diseases [4–26].

One of the methods to non-invasively measure blood flow velocities that are needed for WSS computation is Magnetic Resonance Imaging (MRI) [27, 28]. Application of MRI to flow assessment in cardiovascular diseases began in the middle of the 1980s [28], and within the last 20 years the field of Cardiovascular Magnetic Resonance (CMR) has witnessed major advancements [29]. MRI provides the unique ability to acquire spatially registered blood flow simultaneously with morphological data within a single measurement [30].

The current review has two goals and therefore consists of two parts. First, we aim to give an introduction into MRI-based WSS quantification in large blood vessels. For this purpose, we consider the following topics in the first chapter: WSS as a potential biomarker in cardiovascular diseases, cardiovascular MRI, MR-based WSS quantification methods and their accuracy and validation. References to recent studies on each topic are provided, and several reviews are listed that can be used for further reading.

Our second goal is to present the generic nonlinear regression method for MRI-derived WSS quantification, which is based on the Clauser plot method [31]. The original Clauser plot method is a graphical method to estimate WSS within the logarithmic part [32] of a boundary layer in fully developed turbulent stationary flows. In our earlier work [33], we presented a nonlinear regression method based of the Clauser plot method. We have shown that, although its direct *in vivo* applicability is limited because of the different flow character, the method rendered a valuable approach for accurate MR-based WSS estimates in controllable flow settings. Therefore, the method may serve as helpful approach for validation of MR-based WSS quantification algorithms prior to their clinical application. In the current work, we propose the generic nonlinear regression method, which is an improvement of the initial nonlinear regression method [33]. We provide the detailed description of the method and its validation.

## 1. Quantification of WSS using magnetic resonance imaging

### 1.1. Wall shear stress as a biomarker

WSS has been suggested as a potential biomarker in various cardiovascular diseases including atherosclerosis, aortic stenosis, aneurysms, and bicuspid aortic valve [4–26]. A review by Kathritis et al. [4] presented the definition of WSS, introduced relevant concepts of fluid mechanics, and summarized the various methods that have been used for the assessment of WSS in *in vivo* blood circulation. In a review by Potters et al. [5] the clinical applications of WSS assessment were discussed including an overview of estimated WSS magnitudes in different patient groups at multiple anatomical locations (aorta, carotid arteries, and intracranial vessels). In a review by Kamphuis et al. [1] imaging biomarkers (including WSS) were reviewed that have been shown to distinguish between normal and abnormal flow patterns.

WSS measurements in the aorta of 224 healthy subjects demonstrated that the normal range of thoracic WSS depends on location, decreases with age, and is strongly correlated with velocity, vessel diameter, and radius of curvature of the aortic arch [6]. In [7], normal physiologic correlations between several parameters were investigated: correlations between 1) magnetic resonance elastography (MRE) derived aortic wall stiffness and aortic WSS, and 2) MRE-derived aortic wall stiffness, aortic WSS and age in the abdominal aorta in healthy human subjects. A significant negative correlation was observed between 1) end-systolic MRE-derived aortic wall stiffness and aortic WSS in both axial and circumferential directions, and 2) age and aortic WSS in both axial and circumferential directions.

In a review by Shaaban and Duerinckx [8] in 2000, it was stated that a hypothesis on the key role of low and oscillatory WSS in the initiation and development of atherosclerosis gained popularity. The low shear stress theory challenged the prevailing high shear stress theory, which was associated with the intuitively appealing mechanistic hypothesis that high shear stress damages the endothelium allowing excessive entry of plasma lipoproteins into the wall [9]. The idea of involvement of oscillatory shear developed from [34] where lesion distributions in post-mortem human arteries were studied [9]. In a review by Peiffer et al. [9] in 2013, the low/oscillatory shear theory was claimed to be widely assumed. The goal of [9] was to ascertain that this hypothesis is justified by published data. Therefore, a systematic review of papers that compared the localization of atherosclerotic lesions with the distribution of several hemodynamic indicators (including low WSS, low instantaneous WSS, and low time-averaged WSS) calculated using Computational Fluid Dynamics (CFD) was presented. It was concluded that although many articles claim their results conform to the theory, it has been interpreted in different ways. Longitudinal studies starting from the healthy state, or the collection of average flow metrics derived from large numbers of healthy vessels, both in conjunction with point-by-point comparisons using appropriate statistical techniques, will be necessary to improve understanding of the relation between blood flow and atherogenesis.

In [10], blood flow patterns in the ascending aorta of patients with aortic stenosis were studied and their association with left ventricular remodelling was evaluated. It was found that aortic stenosis leads to abnormal blood flow patterns and peak systolic WSS in the ascending aorta. In [11], blood flow patterns and vessel wall parameters, including WSS, in ascending aorta and aortic arch of patients with dilated ascending aorta and age-matched controls were investigated. It was concluded that an increase in ascending aorta diameter is significantly correlated with a decrease in systolic WSS. In [12], the geometry of aortic arch aneurysms and their relationship with WSS was evaluated to better characterize saccular aneurysms. It was found, for example, that fusiform aneurysms elongated as they dilated, and WSS was lower when the diameter was larger.

Bicuspid aortic valve (BAV) is the most common congenital cardiac disease and it is a foremost risk factor for aortopathies [13]. In [14], it was concluded that an increased and asymmetrically distributed WSS at the aorta wall is related to ascending aortic flow jets, which are influenced by the BAV fusion pattern. In [15], the impact of different BAV cusp pattern fusion on quantitative measures of aortic hemodynamics including the WSS was evaluated. It was concluded that the presence and type of BAV fusion is associated with changes in regional WSS distribution.

In [16], the relationship between WSS and regional aortic tissue remodelling in BAV patients was assessed to determine the influence of regional WSS on the expression of extracellular matrix (ECM) dysregulation. It was found that regions of increased WSS cor-

respond with ECM dysregulation and elastic fiber degeneration in the ascending aorta of BAV patients. The results in [13] suggested that WSS alterations might precede the onset of aortopathy and might contribute to its triggering. Moreover, it was shown that WSS-driven anatomical remodelling, if it exists, is a very slow process [13].

In [17], a large study with 517 subjects was performed to investigate BAV and distinct patterns of expression for WSS on the ascending aorta wall, as stratified by aortic valve phenotype and stenosis severity. Systolic WSS atlases (i. e. a cohort-averaged 3D WSS map which is illustrated on a group-specific aorta surface) were created in order to quantify group-specific WSS patterns in the ascending aorta as a function of aortic valve stenosis severity. It was concluded that distinct WSS patterns exist for BAV patients without aortic valve stenosis. However, BAV patients with significant stenosis exhibit very similar WSS patterns to tricuspid aortic valve patients with stenosis so that a differentiation might be difficult.

In [18], differences in flow patterns and regional axial and circumferential WSS maps for different BAV phenotypes and their correlation with ascending aorta dilatation and morphology were analyzed. It was concluded that the assessment of axial and circumferential WSS components among other parameters may help to better identify patients with a higher risk of aortic dilatation. In [19], a potential association between the magnitude of flow-mediated aortic WSS and medial wall histopathology in BAV patients with aortopathy was investigated. It was found that BAV patients exhibit significantly increased aortic valve-mediated WSS associated with elastic fiber thinning, particularly with aortic valve stenosis and in earlier stages of aortopathy. Elastic fiber thinning correlates with impaired tissue biomechanics. In [23], the effect of the presence of aortic valve stenosis and aortic diameter on peak WSS and surface area of increased WSS in the ascending aorta was evaluated. It was concluded that the extent of increased WSS in the ascending aorta of BAV patients depends on the presence of aortic valve stenosis and aortic dilatation and is most pronounced in the presence of aortic stenosis and a nondilated ascending aorta. In a recent review [20] the latest findings on using WSS as a specific biomarker for risk stratification of BAV patients with aortopathy were presented. The clinical value of WSS was described, and it was stated that WSS has potential to be used as a noninvasive biomarker in risk prediction for bicuspid aortopathy.

In [21], changes in thoracic aortic WSS in asymptomatic patients with Marfan syndrome (MFS) were quantified in comparison to healthy controls. Marfan syndrome, being a genetic disorder of the connective tissue, affects the mechanical properties of the aortic wall and often leads to aortic root dilation, aneurysms, or even dissection [21]. It was found that MFS patients had segmental differences in peak systolic WSS with significantly higher WSS at the inner curvature in the proximal ascending aorta and at the anterior part in the more distal ascending aorta.

WSS can also be used for the analysis of blood flow characteristics after surgery. In [22], the local distribution of systolic WSS was one target parameter in the analysis of blood flow characteristics in the ascending aorta after transcatheter aortic valve replacement (TAVR) in comparison to surgical aortic valve replacement (SAVR) and healthy subjects. Later it was found that TAVR resulted in increased blood flow velocity and WSS in the ascending aorta compared to age- and gender-matched controls [24]. In [26], several parameters including WSS for stented and stentless bioprostheses 1 year after surgical aortic valve replacement were evaluated. It was concluded that stented and stentless aortic valve prostheses exhibit comparable average WSS in the ascending aorta. However, the local flow profiles for stentless prosthesis revealed lower values for WSS.

In a state-of-the-art paper by Garcia et al. [25] it is stated that metrics, such as WSS, had potential to improve characterization of aortic diseases beyond basic flow metrics known to be associated with aortopathy and aortic valve disease.

## 1.2. WSS Quantification via phase contrast MRI

In general, there are three ways to ascertain *in vivo* blood velocities that are needed for WSS computation [4]: 1) invasive methods, 2) non-invasive methods, 3) CFD simulations. Invasive methods typically use intravascular Doppler ultrasound measurements. Non-invasive methods include ultrasound measurements, e. g. via pulsed Doppler ultrasound, and phase-contrast magnetic resonance imaging (PC-MRI), which is the focus of the current paper.

Magnetic resonance imaging (MRI) [27] provides non-invasive and non-ionising methods for accurate, time resolved anatomical depiction of the heart and associated vessels [30]. Applications of MRI for flow assessment in cardiovascular diseases started in the middle of the 1980s, first to measure flow in the heart, and later to assess flow in larger vessels (e. g., aorta or carotid arteries) [28]. The intrinsic sensitivity of the MRI signal to motion provides the unique ability to measure spatially registered blood flow simultaneously with morphological data within a single measurement [30].

MRI flow imaging is based on the so-called phase contrast (PC) technique [28]. Since its initial development in the 1980s, PC-MRI has been widely used in clinical research to visualize and quantify blood flow in the heart, aorta and large vessels [35]. With modern PC-MRI techniques time-resolved (CINE) 3D PC-MRI measurements can be accomplished which provide three-directional velocity encoding and are typically referred to as “4D flow MRI” [35]. In a recent consensus statement by Dyverfeldt et al. [2], the term “4D Flow MRI” or “4D Flow CMR” was recommended to be used.

A review of the state-of-the-art (as of 2015) in Cardiovascular Magnetic Resonance (CMR) PC imaging methodology was presented by Nayak et al. [28]. In a review by Lee et al. [29] CMR research trends and highlights were summarized that were presented at scientific sessions of the annual meeting of the Society for Cardiovascular Magnetic Resonance (SCMR) from 1998 to 2017. It was stated that within the given period, the field of CMR witnessed major advancements in data acquisition speed, image quality, development of novel imaging techniques, application to a broader range of cardiovascular diseases, and the incorporation into consensus statements and clinical practice guidelines.

In a recent review by Allen et al. [36] which aimed on providing a focused update on the clinical and research trends in MRI of the thoracic aorta, it was concluded that with continued improvements in MRI acquisition speed, as well as the growth of MRI-derived biomarkers, clinical use of MRI for the evaluation of thoracic aortic disease will continue to increase. In a review by Gulsin et al. [37], the fundamentals of CMR in assessment of valvular heart disease (VHD) were described and it was concluded that CMR could be used for the comprehensive evaluation of VHD.

Common 2D CINE PC-MRI allows evaluating of blood flow in a single slice, while 4D flow MRI can provide time-resolved information of blood flow in 3D with full volumetric coverage [35]. Studies on WSS assessment based on 4D flow MRI data obtained have been actively performed since the early 2000s [38].

A summary and comparison of advantages and disadvantages of 4D flow MRI compared to 2D CINE PC-MRI was provided in a review by Markl et al. [39]. 4D flow MRI acquires the 3D volume covering entire cardiovascular region of interest, instead of multiple 2D planes

obtained with standard 2D PC-MRI. 2D planes are cumbersome and difficult to position in cases of complex vascular architecture, often requiring multiple acquisitions [39]. Some regions of interest may not be acquired by 2D PC-MRI due to misplaced planes [39], while any arbitrary slice orientation can be reconstructed from 4D flow MRI data set. 4D flow MRI provides higher resolution without loss of signal-to-noise ratio (SNR). The main limitation of 4D flow MRI is a longer measurement time due to volumetric coverage. The accuracy of 4D flow CMR is largely defined by sufficient spatial and temporal resolution, and adequate signal-to-noise ratio (SNR) [2].

In the consensus statement by Dyverfeldt et al. [2], guidelines for the acquisition, analysis, and possible clinical applications of 4D flow MRI in the heart and great vessels (aorta, pulmonary arteries) were provided. It was stated that 4D CMR had enabled more comprehensive access to regions, cardiac phases and directions of pulsatile blood flows through the cavities of the heart and great vessels. Future research and developments in order to address current limitations and ensure data reliability and validity were discussed.

In a review by Kamphuis et al. [1] current applications of 4D flow MRI in the heart and great vessels were discussed, showing its potential as an additional diagnostic modality which could aid in disease management and timing of surgical intervention.

Advancements in 4D flow MRI mainly aim at shortening the long acquisition times, for example, by incorporating novel undersampling strategies such as compressed sensing [40]. 4D flow MRI together with other advanced MRI flow techniques such as real-time flow imaging, 2D multiple-VENC (velocity encoding parameter) PC-MRI, quantification of complex hemodynamic properties (including WSS), and highly accelerated flow imaging were described in a review by Markl et al. [30]. The applications of these advanced MRI flow techniques for the improved evaluation of cardiovascular diseases (including aortic stenosis and aneurysms, atherosclerosis, aortic plaques, congenital heart disease, atrial fibrillation, coronary artery disease) were presented.

### 1.3. MR-based WSS quantification methods

Although blood is a shear-thinning non-Newtonian fluid [41], it exhibits the behavior of a Newtonian fluid with constant viscosity in larger arteries at high shear rates [42]. For viscous incompressible flow of a Newtonian fluid the shear stress tensor at a surface  $\partial\Omega$  is defined using the rate-of-strain-tensor  $\mathbf{D}$  as [43]:

$$\boldsymbol{\tau}|_{\partial\Omega} = 2\mu\mathbf{D}|_{\partial\Omega} = \mu \left[ \nabla\mathbf{u} + (\nabla\mathbf{u})^T \right] |_{\partial\Omega}, \quad (1)$$

where  $\mu$  is the dynamic viscosity,  $\mathbf{u}$  is the fluid velocity. Thus, WSS quantification requires information about the flow domain  $\Omega$ , especially its boundary  $\partial\Omega$ , and the derivative of the blood velocity field  $\nabla\mathbf{u}$  at  $\partial\Omega$ . As described in the previous section, PC-MRI can be used to quantify blood flow velocities, therefore, allowing computation of  $\nabla\mathbf{u}$ .

To our knowledge, the review by Shaaban and Duerinckx [8] was one of the first to summarize then existing MRI-based WSS quantification methods for carotid arteries. A review by Pantos et al. [44] from 2007 was one of the first to report about available literature on *in vivo* WSS quantification in healthy individuals using PC-MRI. In 2014 a review by Potters et al. [5] was published of then existing WSS calculation methods based on velocity-encoded MRI. The basics of velocity-encoded MRI were reviewed and WSS quantification methods from 2D or 3D CINE velocity-encoded MRI measurement data were presented. It was noted that in recent years there has been a trend towards 3D WSS quantification methods.

The comprehensive review of existing methods is out of scope of the current paper, however, a few references to some of the recent works are provided below. Further references can be found in the cited works and in the reviews cited above. MRI-based WSS quantification typically requires two basic steps: first, the identification of the flow domain  $\Omega$ , especially its boundary  $\partial\Omega$ , and second, computation of the derivative of the blood velocity field  $\nabla\mathbf{u}$  at  $\partial\Omega$ . Therefore, these crucial features of methods are highlighted when citing the works below.

The method by Stalder et al. [45] combined B-spline interpolation and Green's theorem to provide optimized quantification of blood flow and vessel wall parameters. In order to ensure that the estimated WSS vector was tangential to the vessel wall, the projection of WSS on the tangential plane was used for the measured WSS [46]. The method [45] has been extensively used in the various later studies [7, 10, 11, 14, 15, 21, 22], where the aortic lumen contours were manually delineated for each analysis 2D plane, and WSS estimation was based on a direct interpolation of the local velocity derivative on the segmented vessel lumen contour.

In [18] double-oblique analysis planes were equally distributed in the ascending aorta, and Mass Research Software (Leiden University Medical Center, Leiden, Netherlands) was used for the location of the analysis planes and manual lumen segmentation. Peak-systolic WSS vectors were calculated by fitting the 3D velocity data with B-splines surfaces and computing velocity derivatives on the segmented vessel lumen [45].

Advances in MRI enabled WSS evaluation not only on a cross section but on the entire volumetric vessel wall even with an arbitrary 3D curvature [38].

In [47], the 3D WSS vector field was decomposed into its axial and circumferential components using a 3D finite element interpolation method [48] and a Laplacian finite element approach. The 3D finite-element method [48] was also used for WSS estimation in [49].

A volumetric WSS calculation method was presented by Potters et al in [50], later this method was used in [51] to compute WSS distributions on the entire 3D luminal surface of carotid arteries. In [16, 17, 19, 23, 24, 26, 52–54], semi-automatic 3D segmentation of the aorta was done using a commercial software package (Materialise Mimics, Leuven, Belgium), and 3D WSS along the aortic lumen surface was calculated using the method [50].

In [12], cross-sectional planes were manually placed perpendicular to the centerline of the aorta and a 3D method [55] was used for MRI-derived WSS calculation. In [56], two methods for improved quantification of *in vivo* WSS in the aortic wall were developed: the Local Planar approach, which operated on 2D planes, and the Global Volumetric approach, which operated on the volumetric data set. The velocity derivatives were computed numerically using a weighted central difference scheme adopted through Sobel filters [57]. In [13], the methods [56] were used, but with B-spline based filters [58] in the Global Volumetric approach.

In [59] the methods to analyze aortic WSS from 4D Flow MRI were classified in two categories. In the first category, analysis planes along the aorta are manually selected, and the vessel cross section is segmented in each plane to explicitly mark the vessel boundary. Then, WSS is evaluated by numerically approximating the change in velocity perpendicular to these boundary regions at each time point. In the second category, semi-automatic segmentation and interpolation are used to generate a 3D mesh of the vessel and subsequently evaluate WSS. The primary limitation of both strategies is the need for full or partial user-input for the aorta segmentation [59]. Therefore, a segmentation-free method was suggested in [59] to visualize and compute WSS throughout the aorta using 4D flow MRI data, where fluid speed was used to enhance visualization of vessel boundaries.

#### 1.4. Accuracy and validation of MR-based WSS quantification methods

It has been shown that in general PC-MRI-based WSS quantification methods tend to underestimate the WSS values [45, 52, 60]. The accuracy of MR-based WSS quantification depends on the accuracy of the boundary identification, the accuracy of the numerical computation of the derivative of the velocity field  $\nabla\mathbf{u}$ , and the PC-MR acquisition parameters [2, 49, 50, 60, 61].

The main factor for the variability of MR-derived WSS is the limited spatial resolution of the acquired data [2, 6, 49, 50, 60, 61]. Partial volume effects act as main confounder to accurately measure blood flow velocity in the proximity of the vessel wall. Furthermore, the velocities close to the boundary are smaller than the velocities occurring further inside so that they are more prone to phase noise because the velocity encoding (VENC) parameter is typically chosen according to the expected maximum velocities to avoid phase aliasing [61]. The temporal resolution of the PC-MR data was demonstrated to have only minor impact on the WSS estimate [49, 61].

Besides confounding effects due to limited spatial resolution, image-based WSS computation is sensitive to the identification of the flow boundary, i. e. correct delineation of the vessel wall [50, 60, 61]. Even small errors in the boundary identification influence the WSS estimate because of the steep velocity gradients at the boundary. In addition, the accuracy of the numerical method to calculate the velocity derivative  $\nabla\mathbf{u}$  might affect the accuracy of the entire WSS computation.

In [62], scan-rescan reproducibility and observer variability of segmental aortic systolic WSS by phase-specific segmentation of 4D flow data acquired in healthy volunteers was investigated. It was found that scan-rescan reproducibility was good for mean systolic WSS for all thoracic aortic regions and moderate for maximum systolic WSS with higher variability in the proximal ascending aorta. The intraobserver and interobserver reproducibility for segmental systolic WSS analysis of maximum systolic WSS and mean systolic WSS was good to excellent. In general, the ascending aortic segments showed more variability in maximum systolic WSS and mean systolic WSS compared to aortic arch or descending aortic segments for scan-rescan, intraobserver and interobserver comparison.

In [52], the reproducibility and interobserver variability of 3D velocity vector fields and 4D-flow-derived WSS in the thoracic aorta averaged over five systolic time frames was investigated in a cohort of healthy subjects. It was concluded that systolic velocity and WSS are reproducible between consecutive visits, with low interobserver variability.

In [63], a velocity field improvement (VFIT) algorithm for denoising 4D flow datasets was presented to improve spatial resolution of velocity and velocity gradient data. This technique was adopted in [6], where a multi-VENC encoding strategy [64] was applied to maximize the velocity-to-noise ratio. It was concluded that accurate 4D-flow-derived WSS measurement is feasible, and a standardized parametric approach for analysis and presentation was given.

In [38], the so-called Reynolds resolution criterion — incorporating spatial resolution, VENC, kinematic viscosity of the working fluid, and SNR — was suggested to assess the accuracy of WSS estimation from 4D flow MRI measurements of the fully-developed, laminar flows in circular tubes. It was noted that it is necessary to investigate the validity of using the same concept in *in vivo* studies.

*In vivo* comparison against current gold standard methods is problematic for many areas of 4D flow MRI, mostly because of the lack of such a standard *in vivo* [2]. Also, reference data is often not available. Some information about *in vivo* WSS values is available from the

literature, but this data is subject-specific and can serve as an approximate estimate only. One solution could be to consider the values derived from the 4D flow data with the highest available spatio-temporal resolution as a reference, as done in [49].

For areas where an *in vivo* gold standard does not exist, controlled steady and pulsatile flow phantom experiments with accurate reference quantification can be used to assess WSS accuracy [2]. As it was stated in [2], in view of the range of commercial and custom-built phantoms, it should be feasible to validate applications by simulating different flow regimes (for example, by varying Reynolds and Womersley numbers), cycle-to-cycle variation and presence of sufficient static tissue for background correction.

The reference data for controllable phantom settings can be also obtained, for example, using CFD simulations or Laser Doppler Velocimetry (LDV) experiments [65, 66]. For some types of flows theoretical WSS values can be calculated using known formulas. For example in [38], the accuracy of velocity measurements and WSS estimations were compared to theoretical results based on the Hagen–Poiseuille law for flows in circular tubes. In the current work, we use the friction factor formula to calculate WSS in fully developed turbulent flows in straight pipes [32].

In the following chapter, we presented the generic nonlinear regression method for improved WSS estimation in fully developed turbulent flows that produce accurate estimates independent from the resolution and may serve as a reliable reference for validation of more generic WSS estimators prior to their clinical applications.

## 2. Generic nonlinear regression method

### 2.1. Logarithmic law of the wall and Clauser plot method

The Clauser plot method estimates the WSS using data from the logarithmic part of the boundary layer in a fully developed turbulent stationary flow. It is a method to estimate WSS within the logarithmic part [32] of a boundary layer in fully developed turbulent stationary flow. The logarithmic boundary layer is the part of the flow domain, where the distance to the wall  $y$  satisfies

$$30 \frac{\nu}{u_\tau} \leq y \leq 100 \frac{\nu}{u_\tau}. \quad (2)$$

Here

$$u_\tau = \sqrt{\frac{\tau_w}{\rho}} \quad (3)$$

is the friction velocity,  $\rho$  is the fluid density,  $\nu$  is the kinematic viscosity.  $\rho$  and  $\nu$  are assumed to be known. There is empirical evidence that the statistical mean velocity  $u$  in the logarithmic layer satisfies the logarithmic law of the wall [32]

$$u(y; u_\tau) = \frac{1}{\kappa} \log \left( \frac{yu_\tau}{\nu} \right) u_\tau + Bu_\tau, \quad (4)$$

where the von Karman constant  $\kappa$  and the constant  $B$  are empirical constants [67–69]. For fixed  $\kappa$  and  $B$  the value of the friction velocity  $u_\tau$  is related to a certain velocity profile  $y \mapsto u(y; u_\tau)$  in the logarithmic boundary layer.

**Original Clauser plot method.** Originally the Clauser plot method was a graphical method for choosing the friction velocity  $u_\tau^*$ , such that the corresponding velocity profile  $u(y; u_\tau^*)$  visually fitted best to the data [31]. The estimate  $\tau_w^*$  of the wall shear stress is obtained using (3) by  $\tau_w^* = (u_\tau^*)^2 \rho$ .

**Initial nonlinear regression method.** In our earlier work [33], we presented and investigated an implementation of the Clauser plot method for estimating WSS in fully developed turbulent stationary flows using PC-MRI velocity measurements. The estimate on the wall shear stress is obtained by solving a nonlinear regression of the velocity profile  $u(y; u_\tau)$  to the data. The logarithmic boundary layer was a priori appropriately selected, which requires information about the friction velocity.

**Generic nonlinear regression method.** In this work we introduce an improved wall shear stress estimator based on the Clauser plot principle. It requires only a rough initial guess on the logarithmic boundary layer and uses different values of the constants  $\kappa$  and  $B$  for the logarithmic law of the wall (4), allowing the method to automatically process data from different fully developed turbulent flows. In the following section the method is presented in detail. Afterwards we apply the method to different fully developed turbulent flows in the circular pipe.

## 2.2. Algorithm

**Calibration: of the von Karman constant  $\kappa$  and constant  $B$ .** The values of the von Karman constant  $\kappa$  and constant  $B$  slightly depend on the present flow conditions such as the geometry and the Reynolds number [67–69]. Values of  $\kappa$  and  $B$  stated in the literature are  $\kappa \in [0.33; 0.45]$  [67, 70, 71] and  $B \in [3.5, 6.15]$  [71]. Obviously, the choice of the constants affects the results of the method. Using non-optimized constants leads to an error of about 5%. To calibrate our method we use nondimensionalized data  $(y_i^+, u_i^+)$ ,  $i = 1, \dots, n$ , of Direct Numerical Simulation (DNS), i. e.  $u_i^+ = u/u_\tau$ ,  $y_i^+ = yu_\tau/\nu$ , and fit the logarithmic law of the wall (4) to the data. Incorporating only data from the logarithmic boundary layer, i. e.  $30 \leq y_i^+ \leq 100$ , we solve

$$(a^*, b^*) = \arg \min_{a, b \in \mathbb{R}^2} \sum_{i=1}^n |a \log(y_i^+) + b - u_i^+|^2$$

and define  $\kappa = 1/a^*$  and  $B = b^*$ . This is done for DNS data [72] of fully developed turbulent pipe flow at  $\text{Re}_1 = 5300$  and  $\text{Re}_2 = 11700$  yielding  $\kappa_1 = 0.3557$ ,  $B_1 = 4.8175$ , and  $\kappa_2 = 0.3876$ ,  $B_2 = 5.0011$  respectively. The values of the constants corresponding to other Reynolds numbers are chosen by linear interpolation or extrapolation accordingly.

**Initialization.** To start the nonlinear regression method for estimating the friction velocity  $u_\tau$  an initial guess  $u_\tau^0$  is required. From the PC-MRI measurements and after segmentation, we have the data  $(y_i, u_i)$ , where  $y_i$  are the distances between the center of a voxel and the wall and  $u_i$  are the corresponding velocity values in these voxels. Reformulating the logarithmic law of the wall (4) yields

$$u(y; u_\tau) = \frac{1}{\kappa} \log(y) u_\tau + \frac{1}{\kappa} \log\left(\frac{u_\tau}{\nu}\right) u_\tau + B u_\tau.$$

Therefore, we fit the data  $(y_i, u_i)$  to the logarithmic ansatz  $u = a \log(y) + b$  by solving the least squares problem

$$(a^*, b^*) = \arg \min_{a, b \in \mathbb{R}^2} \sum_{0.2R < y_i < 0.5R} |a \log(y_i) + b - u_i|^2.$$

The a priori guess on the logarithmic boundary layer  $I^0 = (0.2R, 0.5R)$ , where  $R$  is the pipe radius, is only based on the pipe geometry. The friction velocity is initially estimated using the slope of the regression function only by  $u_\tau^{(0)} = \kappa a^*$ .

**Nonlinear iteration.** Given the current iterate  $u_\tau^{(k)}$  of the friction velocity we define the estimated logarithmic boundary layer  $I^{k+1}$ , according to (2) by

$$I^{k+1} := \left( 30 \frac{\nu}{u_\tau^{(k)}}, 100 \frac{\nu}{u_\tau^{(k)}} \right).$$

Then the following iterate  $u_\tau^{(k+1)}$  is the solution of the linearized problem

$$u_\tau^{(k+1)} = \arg \min_{u_\tau \in \mathbb{R}} \sum_{y_i \in I^{k+1}} \left| u(y_i; u_\tau^{(k)}) + \frac{\partial u}{\partial u_\tau}(y_i; u_\tau^{(k)}) (u_\tau - u_\tau^{(k)}) - u_i \right|^2,$$

where the partial derivative of  $u$  with respect to  $u_\tau$  is given by

$$\frac{\partial u}{\partial u_\tau}(y; u_\tau) = \frac{1}{\kappa} \log\left(\frac{u_\tau}{\nu} y\right) + \frac{1}{\kappa} + B.$$

The termination criterion for the iterative process is chosen as

$$\frac{|u_\tau^{(k+1)} - u_\tau^{(k)}|}{|u_\tau^{(k+1)}|} \leq 10^{-6}.$$

Using the last iterative value  $u_\tau^*$  we define the wall shear stress estimate according to (3) by  $\tau_w^* = (u_\tau^*)^2 \rho$ .

### 3. Methods

Our generic nonlinear regression approach for WSS quantification was tested on a dedicated controllable MR-compatible flow setup as described in [73] using 2D PC-MR velocity measurements carried out in a glass pipe with an inner diameter 25.9 mm. The pipe was placed inside a 3 Tesla whole-body scanner (MAGNETOM Prisma, Siemens Healthineers, Erlangen, Germany) along the magnet's center line. Fully developed turbulent stationary flow was provided at Reynolds numbers of  $Re = 3000, 5370, 8060$ . The flow pump (RMMS1, Sondermann, Köln, Germany) was located outside the MR scanner cabin and connected via plastic hoses and straight in-flow pipes (approximate length: 2 m) to ensure a fully developed flow character. Pure water at room temperature doped with copper sulfate with a concentration of 1 g per liter [74] was used as a fluid for MRI measurements.

Our 2D PC-MR technique was a conventional phase-contrast MRI sequence which is based on a spoiled gradient echo sequence with bipolar velocity encoding along the slice

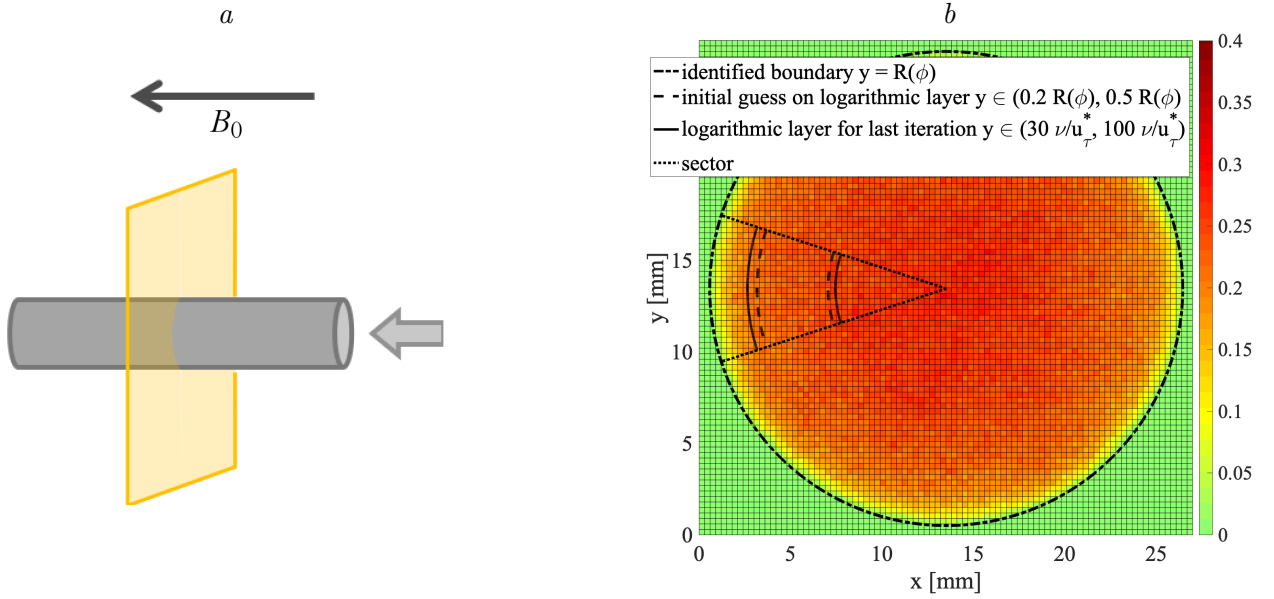


Fig. 1. Experimental setup,  $B_0$  is the direction of the main static magnetic field in the MRI scanner (a); MR velocity measurement data, Reynolds number  $Re = 5370$ , resolution  $0.30 \times 0.30 \text{ mm}^2$ , identified boundary of the flow domain, the sector for  $\varphi_i = 0$ ,  $\Delta\varphi = \pi/10$ , initial guess on logarithmic layer, logarithmic layer for the last iteration (b)

selection direction. 2D PC-MR images were acquired in a plane oriented perpendicular to the pipe axis (i.e. axial slice orientation; Fig. 1, a for different in-plane resolutions (range:  $0.30 \times 0.30$ – $1.00 \times 1.00 \text{ mm}^2$ ) with velocity encoding along the through-plane direction. A VENC of 0.25 m/s was chosen for all Reynolds numbers in order to better resolve the velocities close to the vessel boundary. Phase aliasing because of higher velocities towards the center of the pipe were correct in a post-processing step. Other scan parameters were as follows:  $TR/TE = 17.8 - 18.6 / 5.66 - 5.68 \text{ ms}$ ,  $FOV = 96 \times 96 \text{ mm}^2$ , slice thickness = 3 mm, flip angle =  $7^\circ$ . Signal averaging was performed to obtain sufficient signal-to-noise ratio. For signal reception, a flexible 4-channel coil provided by the scanner manufacturer was wrapped around the glass pipe.

We consider 2D PC-MRI data of a fully developed turbulent pipe flow (see Section 2.3 for the description of the experimental setup), where the flow domain is covered by  $N$  voxels with positions  $\mathbf{x}_i$  and measured velocities  $u_i$ . After the segmentation of the image [75] we obtain the description of the pipe boundary as the radius function  $R$  and the central point of the domain  $\mathbf{x}_0$ , and the wall distances  $y_i$  are computed from the position  $\mathbf{x}_i$ .

To find a local wall shear stress estimate at the boundary point  $\mathbf{x}_i$  positioned at the angle  $\varphi_i$  to the central point, we incorporate only voxels positioned with their central points at the angle  $\varphi \in (\varphi_i - \Delta\varphi, \varphi_i + \Delta\varphi)$ , i.e. in a sector of the width  $2\Delta\varphi$  centered around  $\varphi_i$ . Figure 1, b shows the 2D PC-MRI velocity measurement data of the pipe's cross section with an example of a sector with  $\Delta\varphi = \pi/10$  for the left boundary point at  $\varphi_i = \pi$ .

Two other data sources were used to obtain reference values for validation of the MR-based Clauser plot derived WSS results: (i) measured data from Laser Doppler Velocimetry (LDV) experiments, and (ii) theoretical WSS values calculated with the friction factor formula [32].

The LDV [65, 66] experiments were conducted to provide velocity measurements with much higher spatial resolution compared to the MR data. In brief, LDV measurements use

two coherent laser beams which are focused at a point of interest to create an interference pattern. The flow was seeded with small titanium dioxide particles ( $\sim 1 \mu\text{m}$  diameter) which partly scattered the laser light when travelling through the interference pattern. The same fluid was used for the LDV experiments as for the MRI measurements, except that the flow was not doped with a contrast agent (copper sulfate) but with the small seeding particles. Due to the very small size of the particles, their influence on the flow could be neglected. The flow velocity at the point of interest could then be calculated from the frequency of the scatter light intensity. Finally, cross sectional velocity information was obtained by successively traversing the laser and thus the interference pattern across the entire flow's cross section. To ensure statistical significance, approximately 20.000 particles were captured at each measurement position.

The LDV measurements were carried out at the glass pipes center axis. Refraction of the laser beams was only present along the pipes axial direction and could therefore be corrected in a post-processing step. This method avoided the use of index-matched fluids. For these experiments, an LDV system (Flow Explorer, Dantec Dynamics, Skovlunde, Denmark) was operated in back scatter mode with a wavelength of  $\lambda = 660 \text{ nm}$ , focal length of  $f = 150 \text{ mm}$  and a measurement volume of  $331 \times 49 \times 49 \text{ mm}$ . Although the system was a two component LDV, only the axial velocity component was used. LDV velocity measurements were executed in experimental flow conditions equivalent to the PC-MR measurements for a single Reynolds number of  $\text{Re} = 5370$ . Extreme caution was taken to ensure the same volume flow rate and fluid temperature in both experimental setups. The LDV velocity profile was captured by traversing the laser with a spatial resolution of  $\Delta x = 0.0125 \text{ mm}$ . The WSS values were calculated from the LDV profiles in the same way as described for the PC-MR data via the generic nonlinear regression within the logarithmic region. Reference WSS values for all experimental Reynolds numbers were also calculated using the friction factor formula [32]

$$\tau_w = \frac{1}{8} \lambda \rho u_{\text{mean}}^2, \quad (5)$$

where  $u_{\text{mean}}$  is the mean velocity over the entire cross section of the pipe, the constant  $\lambda$  is the Darcy friction factor, which is known for smoothed wall turbulent pipe flow from the Moody chart [76].

## 4. Results

Figure 2 shows the original Clauser plot for the 2D PC-MRI velocity measurement data ( $\text{Re} = 5370$ , resolution  $0.30 \times 0.30 \text{ mm}^2$ ) for the boundary location  $\varphi = 0$ . Here  $r$  is the normal distance from the wall,  $U(r)$  is the velocity profile,  $U_\infty$  is the velocity in the center of the pipe. Visual estimation provides the WSS value to be approximately equal to  $0.2 \text{ Pa}$ . Using the initial nonlinear regression method [33] the WSS value equal to  $0.1907 \text{ Pa}$  is obtained.

Figure 3 presents 2D PC-MRI velocity measurement data ( $\text{Re} = 5370$ , resolution  $0.30 \times 0.30 \text{ mm}^2$ ), initial guesses and iterative values of the friction velocity  $u_\tau$  up to termination of the iterative process at four boundary locations  $\varphi = 0$ ,  $\varphi = \pi/2$ ,  $\varphi = \pi$ ,  $\varphi = 3\pi/2$  and  $\Delta\varphi = \pi/10$ . The dashed lines indicate the logarithmic sublayer for the last iteration.

Figure 4 shows the LDV velocity measurement data  $\text{Re} = 5370$ , initial guess and iterative values of the friction velocity  $u_\tau$  up to termination of the iterative process, logarithmic sublayer for the last iteration.

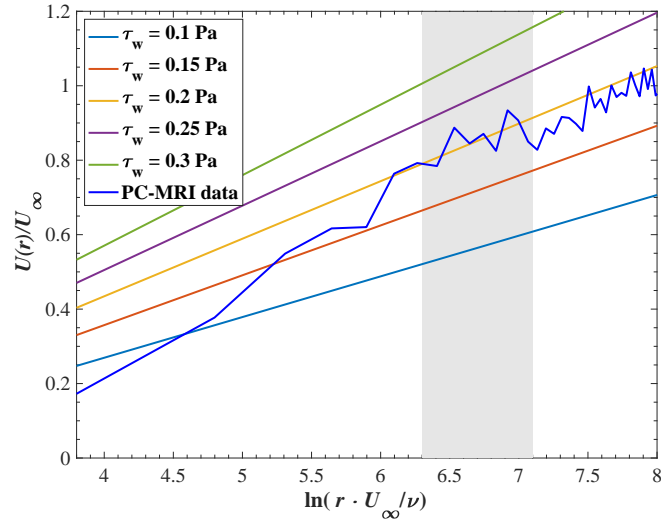


Fig. 2. The original Clauser plot for 2D PC-MRI velocity measurement data ( $Re = 5370$ , resolution  $0.30 \times 0.30 \text{ mm}^2$ ) for the boundary location  $\varphi = 0$

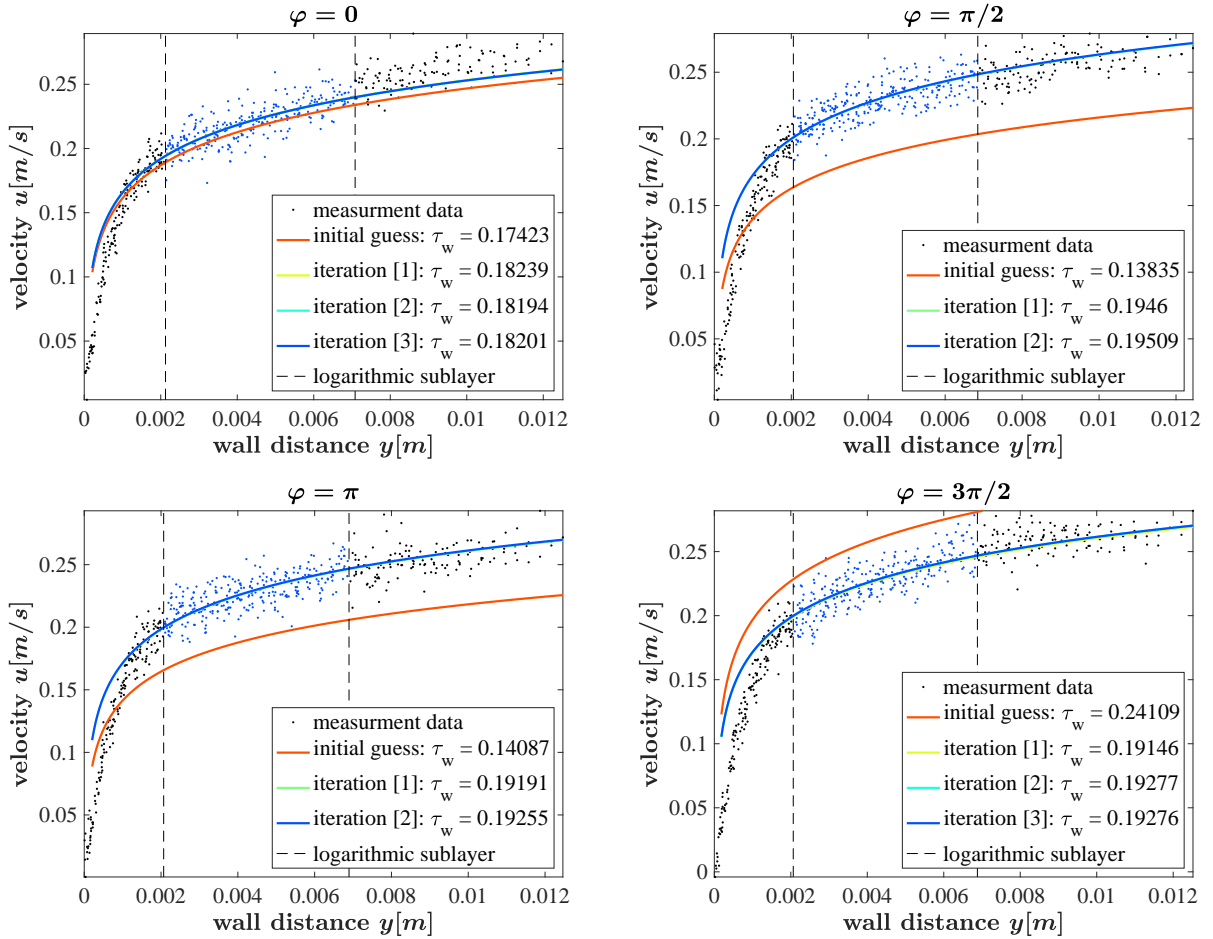


Fig. 3. 2D PC-MRI velocity measurement data ( $Re = 5370$ , resolution  $0.30 \times 0.30 \text{ mm}^2$ ), initial guesses and iterative values of the friction velocity  $u_\tau$  up to termination of the iterative process, and logarithmic sublayers on the last iteration at four boundary locations:  $\varphi = 0$ ,  $\varphi = \pi/2$ ,  $\varphi = \pi$ ,  $\varphi = 3\pi/2$

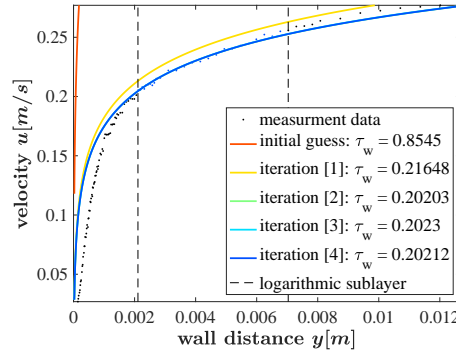


Fig. 4. LDV velocity measurement data, initial guess and iterative values of the friction velocity  $u_\tau$  up to termination of the iterative process, logarithmic sublayer for the last iteration

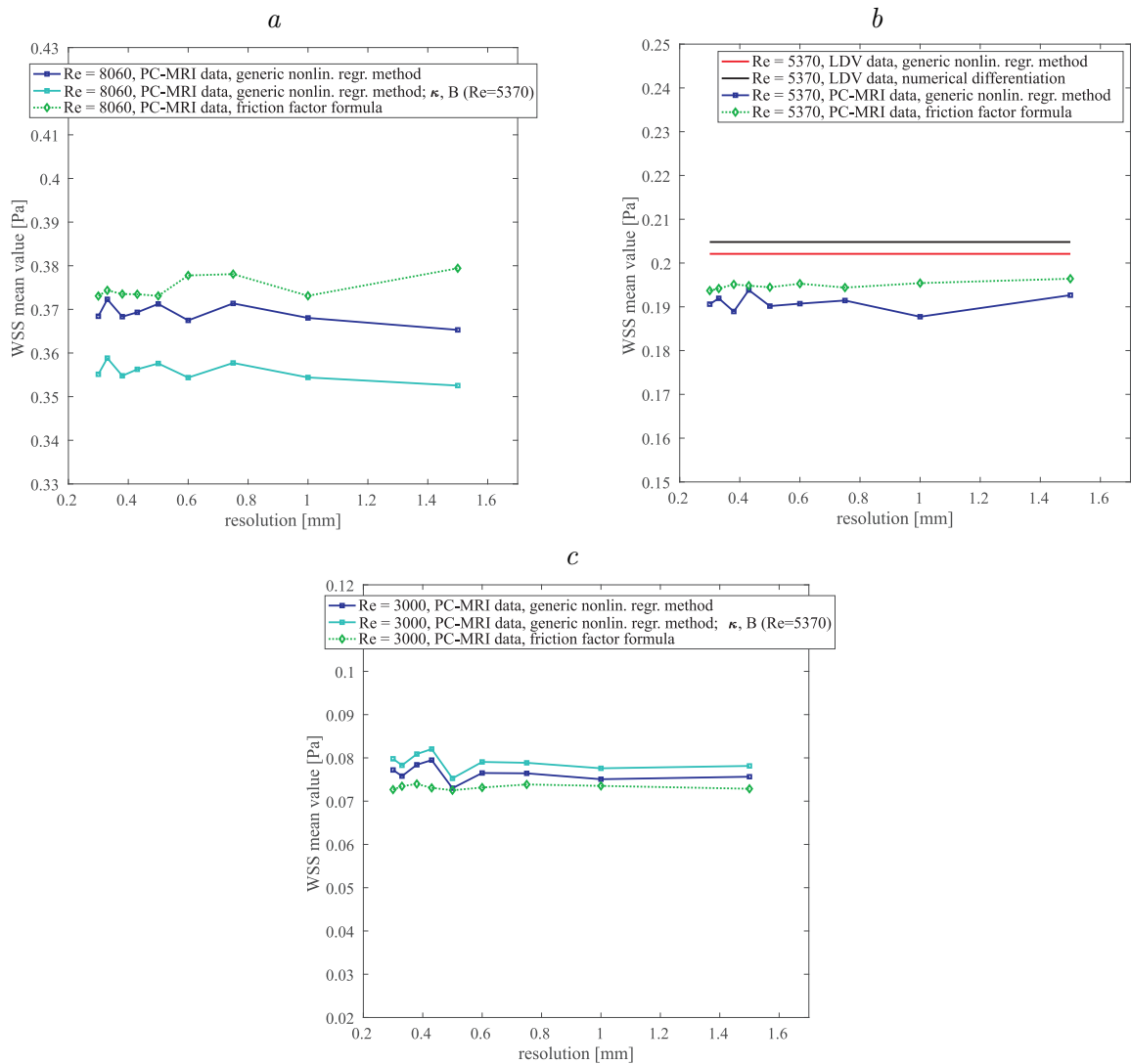


Fig. 5. MR-derived WSS estimates of the generic nonlinear regression method for Reynolds numbers (a) 8060, (b) 5370, and (c) 3000, and different in-plane resolutions; WSS values according to the friction factor formula (5). In (a) and (c): MR-derived WSS estimates of the generic nonlinear regression method with the same values of  $\kappa$  and  $B$  as for  $\text{Re} = 5370$ . In (b): WSS estimates of the generic nonlinear regression method and numerical differentiation from the LDV measurement data for  $\text{Re} = 5370$

Figure 5 shows the MR-derived WSS estimates obtained by the generic nonlinear regression method for the Reynolds numbers 8060, 5370, 3000, and different in-plane resolutions, the reference WSS values according to the friction factor formula (5). The WSS estimates were computed as mean values from the values at four boundary locations  $\varphi = 0$ ,  $\varphi = \pi/2$ ,  $\varphi = \pi$ ,  $\varphi = 3\pi/2$ . For  $\text{Re} = 8060$  and  $\text{Re} = 3000$ , MR-derived WSS estimates by the generic nonlinear regression method with the same values of  $\kappa$  and  $B$  as for  $\text{Re} = 5370$  are presented. For all Reynolds numbers the method shows very little dependency on the spatial resolution of the measurement. It is also seen that a proper choice of the values of  $\kappa$  and  $B$  has significant influence on the accuracy of the WSS estimate.

For  $\text{Re} = 5370$ , the WSS estimates obtained by the generic nonlinear regression method and numerical differentiation from the LDV measurement data are shown for comparison. Due to the difficulties to reproduce identical experimental conditions in MRI and LDV measurements, the flow regimes slightly differed, which might explain the small difference between the WSS estimates obtained from these data and the WSS estimate by the generic nonlinear regression method.

Figure 6, *a* shows the WSS estimates for the Reynolds number  $\text{Re} = 5370$  and spatial resolution of  $0.30 \times 0.30 \text{ mm}^2$  computed by the generic nonlinear regression method at 20 boundary locations equally spaced along the pipe's boundary together with minimal, maximal and mean values. Figure 6, *b* shows contour lines for the same data set, identified boundary of the flow domain and logarithmic layer for the last iteration. At the extreme positions, as for example at the angle  $\varphi = 0$ , where the contour line 0.21 is positioned closer to the pipe's center, the lower WSS values are reached. At  $\varphi = 1$  rad, the both contour lines are positioned closer to the pipe's boundary and closer to each other, higher WSS values are produced.

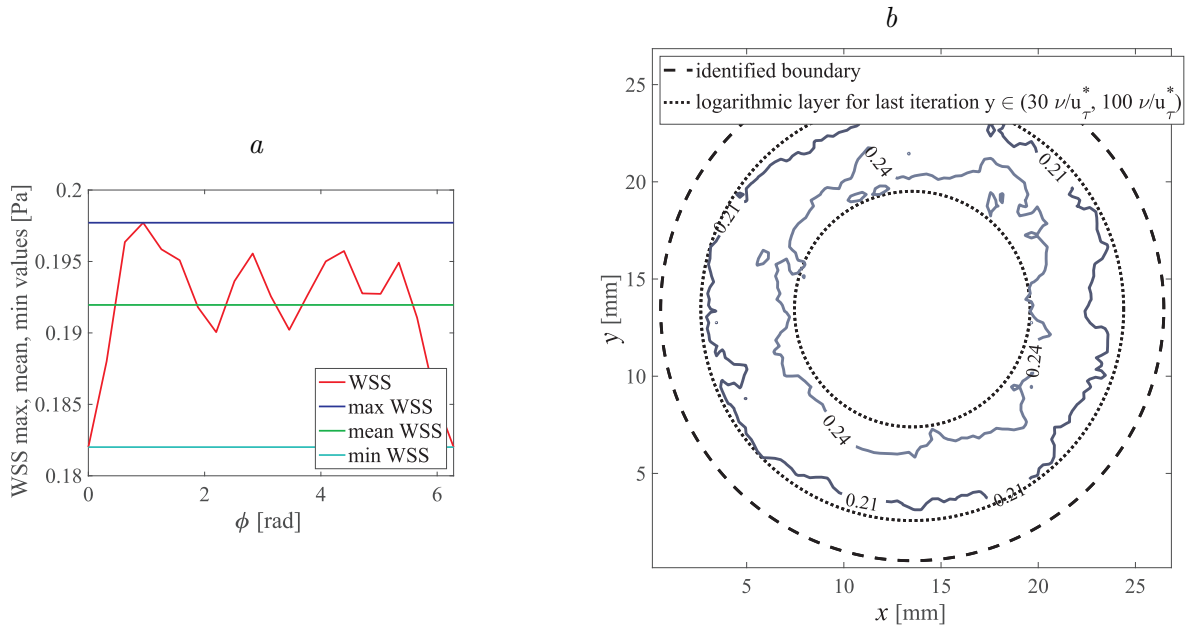


Fig. 6. MR-derived WSS estimates of the generic nonlinear regression method for the ( $\text{Re} = 5370$ , resolution  $0.30 \times 0.30 \text{ mm}^2$ ), at 20 boundary locations equally spaced along the pipe's boundary, maximal, mean, minimal values (*a*); contour lines for MR velocity measurement data ( $\text{Re} = 5370$ , resolution  $0.30 \times 0.30 \text{ mm}^2$ ) identified boundary of the flow domain, logarithmic layer for the last iteration (*b*)

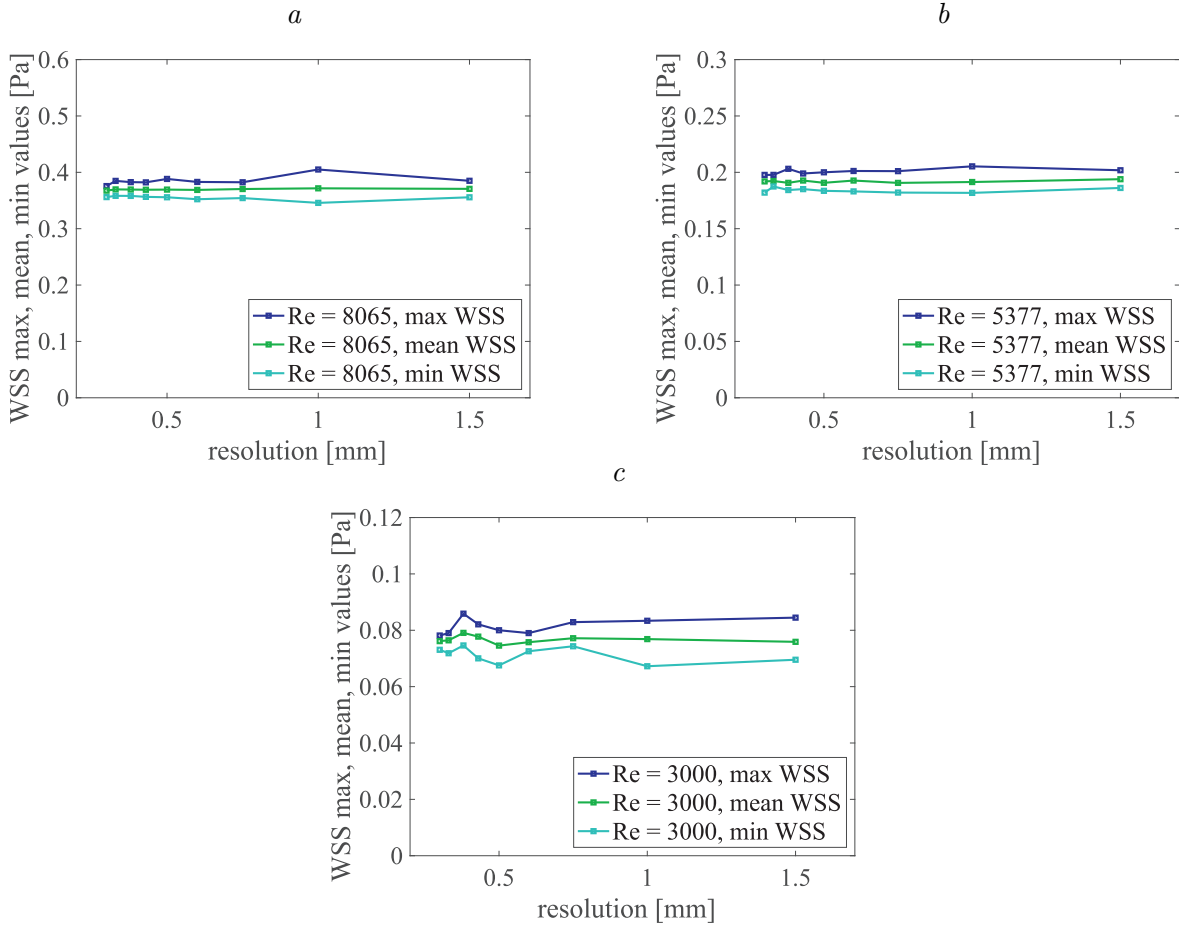


Fig. 7. Maximal, mean, minimal values computed from the MR-derived WSS estimates of the generic nonlinear regression method at 20 boundary locations equally spaced along the pipe's boundary for Reynolds numbers (a) 8060, (b) 5370, and (c) 3000, and different in-plane resolutions

Figure 7 shows these minimal, maximal and mean values for the Reynolds numbers 8060, 5370, 3000, and different in-plane resolutions. For all Reynolds numbers the generic nonlinear regression method shows very little dependency on the spatial resolution of the measurement.

## 5. Discussion

The proposed method solves a nonlinear regression problem, and global convergence of the friction velocity can in general not be expected. However, our numerical tests show that the method is very robust against perturbations in the first guess on the logarithmic boundary region (i.e. the friction velocity value, and consequently, the WSS value) and provides reliable WSS estimates in all cases in very short computation times. The law of the wall is smooth and monotone with respect to the friction velocity, therefore, the Clauser plot estimate, which is based on this law, is stable.

The Clauser plot method has several advantages over the WSS estimators based on numerical differentiation. The first advantage is the use of data from the logarithmic part of the boundary layer, whereas the latter methods require data from the viscous sublayer. Since the logarithmic sublayer spans over a larger range than the viscous sublayer [32], the Clauser

plot method is more robust with respect to low spatial resolution. Additionally, since the logarithmic layer is positioned further from the vessel boundary as the viscous sublayer, the use of velocity values distant from the wall instead of their derivatives directly at the wall reduced the influence of partial volume effects on velocity measurements. Another advantage is that the Clauser plot method does not require the evaluation of velocity derivatives, which allows avoiding problems arising from numerical differentiation of noisy data.

The original Clauser plot method and our initial nonlinear regression method [33] require an a priori estimate on the size of the logarithmic boundary layer, i. e. an a priori estimate on the friction velocity. Our new generic nonlinear regression method requires only a rough first guess about the logarithmic region and iteratively updates its position according to the value of the friction velocity in the current iteration.

The proposed method yields reliable WSS estimates, which are in good accordance to the values computed by the friction factor formula or directly from the LDV data. However, the friction factor formula is restricted to smoothed wall turbulent pipe flows. Further, the LDV data acquisition is expensive and, despite taking a great care about the consistency of experimental setups, the flow situation in LDV measurements differs from the MRI measurements. Therefore, and since the proposed method is able to capture distributed WSS, it is perfectly suited as a benchmark for the assessment of more generic WSS estimators using MRI data. Although the direct *in vivo* applicability of our method is severely limited because of the different flow character [33], it may serve as a helpful approach for validation of MR-based WSS quantification algorithms prior to their clinical application.

**Acknowledgements.** This study was supported by DFG grant numbers DFG HE 1875/30-1, DFG TR 194/56-1, and DFG EG 331/1-1.

## References

- [1] Kamphuis, V.P., Westenberg, J.J.M., van der Palen, R.L.F., Blom, N.A., de Roos, A., van der Geest, R., Elbaz, M.S.M., Roest, A.A.W. Unravelling cardiovascular disease using four dimensional flow cardiovascular magnetic resonance // Intern. J. Cardiovasc. Imaging. 2017. Vol. 33, No. 7. P. 1069–1081. DOI: 10.1007/s10554-016-1031-9.
- [2] Dyverfeldt, P., Bissell, M., Barker, A.J., Bolger, A.F., Carlhäll, C.-J., Ebberts, T., Francios, C.J., Frydrychowicz, A., Geiger, J., Giese, D., Hope, M.D., Kilner, P.J., Kozerke, S., Myerson, S., Neubauer, S., Wieben, O., Markl, M. 4D flow cardiovascular magnetic resonance consensus statement // J. Cardiovasc. Magn. Reson. 2015. Vol. 17, No. 1. P. 72–91. DOI: 10.1186/s12968-015-0174-5.
- [3] Lehoux, S., Tedgui, A. Cellular mechanics and gene expression in blood vessels // Cardiovasc. Biomech. 2003. Vol. 36, No. 5. P. 631–643. DOI: 10.1016/S0021-9290(02)00441-4.
- [4] Katritsis, D., Kaiktsis, L., Chaniotis, A., Pantos, J., Efstathopoulos, E.P., Marmarelis, V. Wall shear stress: theoretical considerations and methods of measurement // Progr. Cardiovasc. Dis. 2007. Vol. 49, No. 5. P. 307–329. DOI: 10.1016/j.pcad.2006.11.001.
- [5] Potters, W.V., Marquering, H.A., VanBavel, E., Nederveen, A.J. Measuring wall shear stress using velocity-encoded MRI // Curr. Cardiovasc. Imaging Rep. 2014. Vol. 7, No. 4. P. 9257–9269. DOI: 10.1007/s12410-014-9257-1.
- [6] Callaghan, F.M., Grieve, S.M. Normal patterns of thoracic aortic wall shear stress measured using four-dimensional flow MRI in a large population // Am. J. Physiol.-Heart Circ. Physiol. 2018. Vol. 315, No. 5. P. H1174–H1181. DOI: 10.1152/ajpheart.00017.2018.

- [7] **Kolipaka, A., Illapani, V.S.P., Kalra, P., Garcia, J., Mo, X., Markl, M., White, R.D.** Quantification and comparison of 4D-flow MRI-derived wall shear stress and MRE-derived wall stiffness of the abdominal aorta // *J. Magn. Reson. Imaging*. 2017. Vol. 45, No. 3. P. 771–778. DOI: 10.1002/jmri.25445.
- [8] **Shaaban, A.M., Duerinckx, A.J.** Wall shear stress and early atherosclerosis // *Am. J. Roentgenol.* 2000. Vol. 174, No. 6. P. 1657–1665. DOI: 10.2214/ajr.174.6.1741657.
- [9] **Peiffer, V., Sherwin, S.J., Weinberg, P.D.** Does low and oscillatory wall shear stress correlate spatially with early atherosclerosis? A systematic review // *Cardiovasc. Res.* 2013. Vol. 99, No. 2. P. 242–250. DOI: 10.1093/cvr/cvt044.
- [10] **von Knobelsdorff-Brenkenhoff, F., Karunaharamoorthy, A., Trauzeddel, R.F., Barker, A.J., Blaszczyk, E., Markl, M., Schulz-Menger, J.** Evaluation of aortic blood flow and wall shear stress in aortic stenosis and its association with left ventricular remodeling // *Circ. Cardiovasc. Imaging*. 2016. Vol. 9, No. 3. P. e004038–e004038. DOI: 10.1161/CIRCIMAGING.115.004038.
- [11] **Bürk, J., Blanke, P., Stankovic, Z., Barker, A., Russe, M., Geiger, J., Frydrychowicz, A., Langer, M., Markl, M.** Evaluation of 3D blood flow patterns and wall shear stress in the normal and dilated thoracic aorta using flow-sensitive 4D CMR // *J. Cardiovasc. Magn. Reson.* 2012. Vol. 14, No. 1. P. 84–95. DOI: 10.1186/1532-429X-14-84.
- [12] **Natsume, K., Shiiya, N., Takehara, Y., Sugiyama, M., Satoh, H., Yamashita, K., Washiyama, N.** Characterizing saccular aortic arch aneurysms from the geometry-flow dynamics relationship // *J. Thorac. Cardiovasc. Surg.* 2017. Vol. 153, No. 6. P. 1413–1420.e1. DOI: 10.1016/j.jtcvs.2016.11.032.
- [13] **Piatti, F., Sturla, F., Bissell, M.M., Pirola, S., Lombardi, M., Nesteruk, I., Della corte, A., Redaelli, A.C.L., Votta, E.** 4D flow analysis of BAV-related fluid-dynamic alterations: evidences of wall shear stress alterations in absence of clinically-relevant aortic anatomical remodeling // *Front. Physiol.* 2017. Vol. 8. P. 441. DOI: 10.3389/fphys.2017.00441.
- [14] **Barker, A.J., Markl, M., Bürk, J., Lorenz, R., Bock, J., Bauer, S., Schulz-Menger, J., von Knobelsdorff-Brenkenhoff, F.** Bicuspid aortic valve is associated with altered wall shear stress in the ascending aorta // *Circ. Cardiovasc. Imaging*. 2012. Vol. 5, No. 4. P. 457–466. DOI: 10.1161/CIRCIMAGING.112.973370.
- [15] **Mahadevia, R., Barker, A.J., Schnell, S., Entezari, P., Kansal, P., Fedak, P.W.M., Malaisrie, S.C., McCarthy, P., Collins, J., Carr, J., Markl, M.** Bicuspid aortic cusp fusion morphology alters aortic three-dimensional outflow patterns, wall shear stress, and expression of aortopathy // *Circulation*. 2014. Vol. 129, No. 6. P. 673–682. DOI: 10.1161/CIRCULATIONAHA.113.003026.
- [16] **Guzzardi, D.G., Barker, A.J., van Ooij, P., Malaisrie, S.C., Puthumana, J.J., Belke, D.D., Mewhort, H.E.M., Svystonyuk, D.A., Kang, S., Verma, S., Collins, J., Carr, J., Bonow, R.O., Markl, M., Thomas, J.D., McCarthy, P.M., Fedak, P.W.M.** Valve-related hemodynamics mediate human bicuspid aortopathy: Insights from wall shear stress mapping // *J. Am. Coll. Cardiol.* 2015. Vol. 66, No. 8. P. 892–900. DOI: 10.1016/j.jacc.2015.06.1310.
- [17] **van Ooij, P., Markl, M., Collins, J.D., Carr, J.C., Rigsby C., Bonow, R.O., Malaisrie, S.C., McCarthy, P.M., Fedak, P.W.M., Barker, A.J.** Aortic valve stenosis alters expression of regional aortic wall shear stress: New insights from a 4-dimensional flow magnetic resonance imaging study of 571 subjects // *J. Am. Heart Assoc.* 2017. Vol. 6, No. 9. P. e005959. DOI: 10.1161/JAHA.117.005959.

- [18] **Rodríguez-Palomares, J.F., Dux-Santoy, L., Guala, A., Kale, R., Maldonado, G., Teixidó-Turá, G., Galian, L., Huguet, M., Valente, F., Gutiérrez, L., González-Alujas, T., Johnson, K.M., Wieben, O., García-Dorado, D., Evangelista, A.** Aortic flow patterns and wall shear stress maps by 4D-flow cardiovascular magnetic resonance in the assessment of aortic dilatation in bicuspid aortic valve disease // *J. Cardiovasc. Magn. Reson.* 2018. Vol. 20, No. 1. P. 28. DOI: 10.1186/s12968-018-0451-1.
- [19] **Bollache, E., Guzzardi, D.G., Sattari, S., Olsen, K.E., Di Martino, E.S., Malaisrie, S.C., van Ooij, P., Collins, J., Carr, J., McCarthy, P.M., Markl, M., Barker, A.J., Fedak, P.W.M.** Aortic valve-mediated wall shear stress is heterogeneous and predicts regional aortic elastic fiber thinning in bicuspid aortic valve-associated aortopathy // *J. Thorac. Cardiovasc. Surg.* 2018. Vol. 156, No. 6. P. 2112–2120.e2. DOI: 10.1016/j.jtcvs.2018.05.095.
- [20] **Fatehi Hassanabad, A., Garcia, J., Verma, S., White, J.A., Fedak, P.W.M.** Utilizing wall shear stress as a clinical biomarker for bicuspid valve-associated aortopathy // *Curr. Opin. Cardiol.* 2019. Vol. 34, No. 2. P. 124–131. DOI: 10.1097/HCO.0000000000000601.
- [21] **Geiger, J., Arnold, R., Herzer, L., Hirtler, D., Stankovic, Z., Russe, M., Langer, M., Markl, M.** Aortic wall shear stress in Marfan syndrome // *Magn. Reson. Med.* 2013. Vol. 70, No. 4. P. 1137–1144. DOI: 10.1002/mrm.24562.
- [22] **Trauzeddel, R.F., Löbe, U., Barker, A.J., Gelsinger, C., Butter, C., Markl, M., Schulz-Menger, J., von Knobelsdorff-Brenkenhoff, F.** Blood flow characteristics in the ascending aorta after TAVI compared to surgical aortic valve replacement // *Intern. J. Cardiovasc. Imaging.* 2016. Vol. 32, No. 3. P. 461–467. DOI: 10.1007/s10554-015-0792-x.
- [23] **Farag, E.S., van Ooij, P., Planken, R.N., Dukker, K.C.P., de Heer, F., Bouma, B.J., Robbers-Visser, D., Groenink, M., Nederveen, A.J., de Mol, B.A.J.M., Kluin, J., Boekholdt, S.M.** Aortic valve stenosis and aortic diameters determine the extent of increased wall shear stress in bicuspid aortic valve disease // *J. Magn. Reson. Imaging.* 2018. Vol. 48, No. 2. P. 522–530. DOI: 10.1002/jmri.25956.
- [24] **Farag, E.S., Vendrik, J., van Ooij, P., Poortvliet, Q.L., van Kesteren, F., Wollersheim, L.W., Kaya, A., Driessen, A.H.G., Piek, J.J., Koch, K.T., Baan, J., Planken, R.N., Kluin, J., Nederveen, A.J., de Mol, B.A.J.M.** Transcatheter aortic valve replacement alters ascending aortic blood flow and wall shear stress patterns: A 4D flow MRI comparison with age-matched, elderly controls // *Eur. Radiol.* 2019. Vol. 29, No. 3. P. 1444–1451. DOI: 10.1007/s00330-018-5672-z.
- [25] **Garcia, J., Barker, A.J., Markl, M.** The role of imaging of flow patterns by 4D flow MRI in aortic stenosis // *JACC Cardiovasc. Imaging.* 2019. Vol. 12, No. 2. P. 252–266. DOI: 10.1016/j.jcmg.2018.10.034.
- [26] **van Kesteren, F., Wollersheim, L.W., Baan Jr., J., Nederveen, A.J., Kaya, A., Boekholdt, S.M., de Mol, B.A., van Ooij, P., Planken, R.N.** Four-dimensional flow MRI of stented versus stentless aortic valve bioprostheses // *Eur. Radiol.* 2018. Vol. 28, No. 1. P. 257–264. DOI: 10.1007/s00330-017-4953-2.
- [27] **McRobbie, D.W., Moore, E.A., Graves, M.J., Prince, M.R.** MRI from picture to proton. 3rd Edition. Cambridge University Press, 2017. 400 p.
- [28] **Nayak, K.S., Nielsen, J.-F., Bernstein, M.A., Markl, M., Gatehouse, P.D., Botnar, R.M., Saloner, D., Christine Lorenz, C., Wen, H., Hu, B.S., Epstein, F.H., Oshinski, J.N., Raman, S.V.** Cardiovascular magnetic resonance phase contrast imaging // *J. Cardiovasc. Magn. Reson.* 2015. Vol. 17, No. 1. P. 71–97. DOI: 10.1186/s12968-015-0172-7.

- [29] Lee, D.C., Markl, M., Dall’Armellina, E., Han, Y., Kozerke, S., Kuehne, T., Nielles-Vallespin, S., Messroghli, D., Patel, A., Schaeffter, T., Simonetti, O., Valente, A.M., Weinsaft, J.W., Wright, G., Zimmerman, S., Schulz-Menger, J. The growth and evolution of cardiovascular magnetic resonance: a 20-year history of the Society for Cardiovascular Magnetic Resonance (SCMR) annual scientific sessions // *J. Cardiovasc. Magn. Reson.* 2018. Vol. 20, No. 1. P. 8–19. DOI:10.1186/s12968-018-0429-z.
- [30] Markl, M., Schnell, S., Wu, C., Bollache, E., Jarvis, K., Barker, A.J., Robinson, J.D., Rigsby, C.K. Advanced flow MRI: emerging techniques and applications // *Clin. Radiol.* 2016. Vol. 71, No. 8. P. 779–795. DOI:10.1016/j.crad.2016.01.011.
- [31] Clauser, F.H. The turbulent boundary layer // *Advances in Applied Mechanics / Dryden, H.L., von Kármán, Th. (Eds). Elsevier, 1956. Vol. 4. P. 1–51. DOI:10.1016/S0065-2156(08)70370-3.*
- [32] Schlichting, H., Gersten, K. *Boundary-layer theory.* 9rd Edition. Berlin; Heidelberg: Springer-Verlag, 2017. 814 p.
- [33] Shokina, N., Bauer, A., Teschner, G., Buchenberg, W.B., Tropea, C., Egger, H., Hennig, J., Krafft, A.J. MR-based wall shear stress measurements in fully developed turbulent flow using the Clauser plot method // *J. Magn. Reson.* 2019. Vol. 305. P. 16–21. DOI:10.1016/j.jmr.2019.05.009.
- [34] Ku, D.N., Giddens, D.P., Zarins, C.K., Glagov, S. Pulsatile flow and atherosclerosis in the human carotid bifurcation. Positive correlation between plaque location and low oscillating shear stress // *Arterioscler.* 1985. Vol. 5, No. 3. P. 293–302.
- [35] Stankovic, Z., Allen, B.D., Garcia, J., Jarvis, K.B., Markl, M. 4D flow imaging with MRI // *Cardiovasc. Diagn. Ther.* 2014. Vol. 4, No. 2. P. 173–192. DOI:10.3978/j.issn.2223-3652.2014.01.02.
- [36] Allen, B.D., Syed, A.A., Bollache, E., Keller, E.J., Barker, A.J., Rose, M.J., Jarvis, K.B., Schnell, S., Markl, M., Carr, J.C., Collins, J.D. Cardiovascular MRI in thoracic aortopathy: A focused review of recent literature updates // *Curr. Radiol. Rep.* 2017. Vol. 5, No. 10. P. 50–59. DOI:10.1007/s40134-017-0246-4.
- [37] Gulsin, G.S., Singh, A., McCann, G.P. Cardiovascular magnetic resonance in the evaluation of heart valve disease // *BMC Med. Imaging.* 2017. Vol. 17, No. 1. P. 67–81. DOI:10.1186/s12880-017-0238-0.
- [38] Ko, S., Yang, B., Cho, J.-H., Lee, J., Song, S. Novel and facile criterion to assess the accuracy of WSS estimation by 4D flow MRI // *Med. Image Anal.* 2019. Vol. 53. P. 95–103. DOI:10.1016/j.media.2019.01.009.
- [39] Markl, M., Schnell, S., Barker, A.J. 4D flow imaging: Current status to future clinical applications // *Curr. Cardiol. Rep.* 2014. Vol. 16, No. 5. P. 481–490. DOI:10.1007/s11886-014-0481-8.
- [40] Ma, L.E., Markl, M., Chow, K., Huh, H., Forman, C., Vali, A., Greiser, A., Carr, J., Schnell, S., Barker, A.J. Aortic 4D flow MRI in 2 minutes using compressed sensing, respiratory controlled adaptive k-space reordering, and inline reconstruction // *Magn. Reson. Med.* 2019. Vol. 81, No. 6. P. 3675–3690. DOI:10.1002/mrm.27684.
- [41] Irgens, F. *Rheology and non-Newtonian fluids.* 1st Edition. Springer International Publishing, 2014. 190 p.
- [42] Chandran, K.B., Rittgers, S.E., Yoganathan, A.P. *Biofluid mechanics: the human circulation.* 2nd Edition. CRC Press, 2012. 451 p.
- [43] Warsi, Z.U.A. *Fluid dynamics: theoretical and computational approaches.* 3rd Edition. CRC Press, 2005. 872 p.

- [44] **Pantos, I., Patatoukas, G., Efstathopoulos, E.P., Katritsis, D.** In vivo wall shear stress measurements using phase-contrast MRI // *Expert. Rev. Cardiovasc. Ther.* 2007. Vol. 5, No. 5. P. 927–938. DOI: 10.1586/14779072.5.5.927.
- [45] **Stalder, A.F., Russe, M.F., Frydrychowicz, A., Bock, J., Hennig, J., Markl, M.** Quantitative 2D and 3D phase contrast MRI: Optimized analysis of blood flow and vessel wall parameters // *Magn. Reson. Med.* 2008. Vol. 60, No. 5. P. 1218–1231. DOI: 10.1002/mrm.21778.
- [46] **Papathanasopoulou, P., Zhao, S., Köhler, U., Robertson, M.B., Long, Q., Hoskins, P., Xu, Y.X., Marschall, I.** MRI measurement of time-resolved wall shear stress vectors in a carotid bifurcation model, and comparison with CFD predictions // *J. Magn. Reson. Imaging.* 2003. Vol. 17, No. 2. P. 153–162. DOI: 10.1002/jmri.10243.
- [47] **Sotelo, J., Dux-Santoy, L., Guala, A., Rodríguez-Palomares, J., Evangelista, A., Sing-Long, C., Urbina, J., Mura, J., Hurtado, D.E., Uribe, S.** 3D axial and circumferential wall shear stress from 4D flow MRI data using a finite element method and a laplacian approach // *Magn. Reson. Med.* 2018. Vol. 79, No. 5. P. 2816–2823. DOI: 10.1002/mrm.26927.
- [48] **Sotelo, J., Urbina, J., Valverde, I., Tejos, C., Irarrázaval, P., Andia, M.E., Hurtado, D.E., Uribe, S.** 3D quantification of wall shear stress and oscillatory shear index using a finite-element method in 3D CINE PC-MRI data of the thoracic aorta // *IEEE Trans. Med. Imaging.* 2016. Vol. 35, No. 6. P. 1475–1487. DOI: 10.1109/TMI.2016.2517406.
- [49] **Montalba, C., Urbina, J., Sotelo, J., Andia, M.E., Tejos, C., Irarrázaval, P., Hurtado, D.E., Valverde, I., Uribe, S.** Variability of 4D flow parameters when subjected to changes in MRI acquisition parameters using a realistic thoracic aortic phantom // *Magn. Reson. Med.* 2017. Vol. 79, No. 4. P. 1882–1892. DOI: 10.1002/mrm.26834.
- [50] **Potters, W.V., Ooij, P., Marquering, H., van Bavel, E., Nederveen, A.J.** Volumetric arterial wall shear stress calculation based on cine phase contrast MRI // *J. Magn. Reson. Imaging.* 2015. Vol. 41, No. 2. P. 505–516. DOI: 10.1002/jmri.24560.
- [51] **Cibis, M., Potters, W.V., Gijzen, F.J.H., Marquering, H., van Bavel, E., van der Steen, A.F.W., Nederveen, A.J., Wnetzel, J.J.** Wall shear stress calculations based on 3D cine phase contrast MRI and computational fluid dynamics: a comparison study in healthy carotid arteries // *NMR Biomed.* 2014. Vol. 27, No. 7. P. 826–834. DOI: 10.1002/nbm.3126.
- [52] **van Ooij, P., Powell, A.L., Potters, W.V., Carr, J.C., Markl, M., Barker, A.J.** Reproducibility and interobserver variability of systolic blood flow velocity and 3D wall shear stress derived from 4D flow MRI in the healthy aorta // *J. Magn. Reson. Imaging.* 2016. Vol. 43, No. 1. P. 236–248. DOI: 10.1002/jmri.24959.
- [53] **van Ooij, P., Potters, W.V., Nederveen, A.J., Allen, B.D., Collins, J., Carr, J., Malasrie, S.C., Markl, M., Barker, A.J.** A methodology to detect abnormal relative wall shear stress on the full surface of the thoracic aorta using four-dimensional flow MRI // *Magn. Reson. Med.* 2015. Vol. 73, No. 3. P. 1216–1227. DOI: 10.1002/mrm.25224.
- [54] **van Ooij, P., Potters, W.V., Collins, J., Carr, M., Carr, J., Malasrie, S.C., Fedak, P.W.M., McCarthy, P.M., Markl, M., Barker, A.J.** Characterization of abnormal wall shear stress using 4D flow MRI in human bicuspid aortopathy // *Ann. Biomed. Eng.* 2015. Vol. 43, No. 6. P. 1385–1397. DOI: 10.1007/s10439-014-1092-7.
- [55] **Isoda, H., Ohkura, Y., Kosugi, T., Hirano, M., Alley, M.T., Bammer, R., Pelc, N.J., Namba, H., Sakahara, H.** Comparison of hemodynamics of intracranial aneurysms between MR fluid dynamics using 3D cine phase-contrast MRI and MR-based computational fluid dynamics // *Neuroradiology.* 2010. Vol. 52, No. 10. P. 913–920. DOI: 10.1007/s00234-009-0634-4.

- [56] **Piatti, F., Pirola, S., Bissell, M., Nesteruk, I., Sturla, F., Della Corte, A., Redaelli, A., Votta, E.** Towards the improved quantification of in vivo abnormal wall shear stresses in BAV-affected patients from 4D-flow imaging: Benchmarking and application to real data // *J. Biomech.* 2017. Vol. 50. P. 93–101. DOI: 10.1016/j.jbiomech.2016.11.044.
- [57] **Shih, F.Y.** Image processing and pattern recognition: fundamentals and techniques. NY: IEEE Press, 2010. 537 p.
- [58] **Hast, A.** Simple filter design for first and second order derivatives by a double filtering approach // *Pattern Recognit. Lett.* 2014. Vol. 42. P. 65–71. DOI: 10.1016/j.patrec.2014.01.014.
- [59] **Masutani, E.M., Contijoch, F., Kyubwa, E., Cheng, J., Alley, M.T., Vasana-wala, S., Hsiao, A.** Volumetric segmentation-free method for rapid visualization of vascular wall shear stress using 4D flow MRI // *Magn. Reson. Med.* 2018. Vol. 80, No. 2. P. 748–755. DOI: 10.1002/mrm.27159.
- [60] **Petersson, S., Dyverfeldt, P., Ebbers, T.** Assessment of the accuracy of MRI wall shear stress estimation using numerical simulations // *J. Magn. Reson. Imaging.* 2012. Vol. 36, No.1. P. 128–138. DOI: 10.1002/jmri.23610.
- [61] **Zimmermann, J., Demedts, D., Mirzaee, H., Ewert, P., Stern, H., Meierhofer, C., Menze, B., Hennemuth, A.** Wall shear stress estimation in the aorta: Impact of wall motion, spatiotemporal resolution, and phase noise // *J. Magn. Reson. Imaging.* 2018. Vol. 48, No. 3. P. 718–728. DOI: 10.1002/jmri.26007.
- [62] **van der Palen, R.L.F., Roest, A.A.W., van den Boogaard, P.J., de Roos, A., Blom, N.A., Westenberg, J.J.M.** Scan-rescan reproducibility of segmental aortic wall shear stress as assessed by phase-specific segmentation with 4D flow MRI in healthy volunteers // *MAGMA.* 2018. Vol. 31, No. 5. P. 653–663. DOI: 10.1007/s10334-018-0688-6.
- [63] **Callaghan, F.M., Grieve, S.M.** Spatial resolution and velocity field improvement of 4D-flow MRI // *Magn. Reson. Med.* 2017. Vol. 78, No. 5. P. 1959–1968. DOI: 10.1002/mrm.26557.
- [64] **Callaghan, F.M., Kozor, R., Sherrah, A.G., Vallely, M., Celermajer, D., Figg-tree, G.A., Grieve, S.M.** Use of multi-velocity encoding 4D flow MRI to improve quantification of flow patterns in the aorta // *J. Magn. Reson. Imaging.* 2016. Vol. 43, No. 2. P. 352–363. DOI: 10.1002/jmri.24991.
- [65] **Durst, F., Melling, A., Whitelaw, J.H.** Principles and practice of laser doppler anemometry. Academic Press, 1976. 412 p.
- [66] **Albrecht, H.-E., Damaschke, N., Borys, M., Tropea, C.** Laser doppler and phase doppler measurement techniques. Berlin; Heidelberg: Springer-Verlag, 2003. 738 p.
- [67] **Bailey, S.C.C., Vallikivi, M., Hultmark, M., Smits, A.J.** Estimating the value of von Kármán’s constant in turbulent pipe flow // *J. Fluid Mech.* 2014. Vol. 749. P. 79–98. DOI: 10.1017/jfm.2014.208.
- [68] **Segalini, A., Örlü, R., Alfredsson, P.H.** Uncertainty analysis of the von Kármán constant // *Exp. Fluids* 2013. Vol. 54, No. 2. P. 1460–1469. DOI: 10.1007/s00348-013-1460-3.
- [69] **Klewicki, J.C., Saric,, W.S., Marusic I., Eaton J.K.** Wall-bounded flow // Springer Handbook of Experimental Fluid Mechanics. 1st Edition. / C. Tropea, A. Yarin, J.F. Foss. (Eds). Berlin; Heidelberg: Springer-Verlag, 2007. P. 871–908.
- [70] **Trinh, K.T.** On the Karman constant. 2010. arXiv:1007.0605. Available at: <https://arxiv.org/abs/1007.0605>
- [71] **Zanoun, E.-S., Durst, F., Nagib, H.** Evaluating the law of the wall in two-dimensional fully developed turbulent channel flows // *Phys. Fluids.* 2003. Vol. 15, No. 10. P. 3079–3089. DOI: 10.1063/1.1608010.

- 
- [72] **El Khoury, G.K., Schlatter, P., Noorani, A., Fischer, P.F., Brethouwer, G., Johansson, A.V.** Direct numerical simulation of turbulent pipe flow at moderately high Reynolds numbers // *Flow Turbul. Combust.* 2013. Vol. 91, No. 3. P. 475–495. DOI: 10.1007/s10494-013-9482-8.
- [73] **Bauer, A., Wegt, S., Bopp, M., Jakirlic, S., Tropea, C., Krafft, A.J., Shokina, N., Hennig, J., Teschner, G. Egger, H.** Comparison of wall shear stress estimates obtained by laser Doppler velocimetry, magnetic resonance imaging and numerical simulations // *Exp. Fluids.* 2019. Vol. 60. P. 112–128. DOI: 10.1007/s00348-019-2758-6
- [74] **Schenck, J.F.** The role of magnetic susceptibility in magnetic resonance imaging: MRI magnetic compatibility of the first and second kinds // *Med. Phys.* 1996. Vol. 23, No. 6. P. 815–850. DOI: 10.1118/1.597854.
- [75] **Egger, H., Teschner, G.** On the stable estimation of flow geometry and wall shear stress from magnetic resonance images // *Inverse Probl.* 2018. DOI: 10.1088/1361-6420/ab23d5. (Accepted).
- [76] **Moody, L.F.** Friction factors for pipe flows // *Trans. Am. Soc. Mech. Eng.* 1944. Vol. 66. P. 671–678.

*Received June 10, 2019*